aerospace

MDPI

Article

Downwash-Aware Design of a Long-Reach Aerial Manipulator for Multirotor UAVs

Boyang Jiang [1], Zhongjing Ren [1,2,3,4,*], Xicai Li [5] and Aibin Yang [4]

[1] School of Mechanical Engineering, Shandong University, Jinan 250061, China; 202300161048@sdu.edu.cn
[2] Shenzhen Research Institute of Shandong University, Shenzhen 518057, China
[3] School of Electrical and Information Engineering, Lanzhou University of Technology, Lanzhou 730050, China
[4] Binzhou Institute of Technology, Binzhou 256600, China; y15169565392@163.com
[5] School of Electronic Science and Engineering, Nanjing University, Nanjing 210023, China; lixicai@nju.edu.cn
* Correspondence: zren@sdu.edu.cn

Abstract

Aerial manipulation tasks performed by multirotor unmanned aerial vehicles (UAVs) are often constrained by rotor-induced downwash, which generates a concentrated high-momentum axial core capable of destabilizing lightweight manipulators and payloads. This paper proposes a downwash-aware design framework for a long-reach, three-degree-of-freedom (3-DOF) aerial manipulator explicitly optimized to mitigate aerodynamic disturbances. The framework integrates CFD-based characterization of the rotor downwash, forward-kinematic modeling, workspace reconstruction, and experimental validation under controlled and real-flight conditions to ensure that the end-effector operates outside the strong-disturbance zone. Link lengths of 0.40 m and 0.80 m were selected to balance operational reach, aerodynamic safety, and platform stability. A controlled measurement setup was established for validation of the CFD numerical model, where the UAV was laterally fixed on a rigid support frame to eliminate flight-induced motion. The experimental results on the velocities at targeted locations show a good agreement with the CFD-predicted velocity profiles, confirming the reliability of the flow-field prediction model. A prototype integrated with a six-rotor UAV was experimentally validated under real flight conditions, demonstrating stable takeoff, manipulator deployment, and retraction, with a visually observable reduction in end-effector oscillation tendency. Several representative grasping configurations where the airflow velocity at the end-effector remained below the threshold of 1 m/s, or a weak-disturbance region, were identified and achieved via manipulation of the UAV system. We envision promising applications of the downwash-aware design of multirotor UAVs with aerial manipulator in high-altitude sampling, precision harvesting, and other contact-intensive aerial manipulation tasks.

Keywords: aerial manipulation; long-reach manipulator; rotor downwash; multirotor UAV; workspace optimization

Check for updates

Academic Editor: Gokhan Inalhan

Received: 14 April 2026
Revised: 11 May 2026
Accepted: 15 May 2026
Published: 30 May 2026

Copyright: © 2026 by the authors. Licensee MDPI, Basel, Switzerland. This article is an open access article distributed under the terms and conditions of the Creative Commons Attribution (CC BY) license.

1. Introduction

Over the past decade, UAVs have achieved remarkable technological advancements [1] and have been extensively applied in various civilian and industrial scenarios, including power line inspection [2], agricultural monitoring [3], logistics and parcel delivery [4], search and rescue missions [5], and infrastructure asset management [6]. Despite these developments, most existing UAV platforms are primarily optimized for perception and transportation tasks [7], with limited capability to perform stable physical interaction with

the environment [8]. Enabling aerial robots to execute dexterous manipulation tasks thus represents a critical step toward expanding their operational functionality beyond passive observation and payload transport [9].

Aerial manipulation platforms equipped with articulated robotic arms constitute a typical realization of such dexterous aerial operations. This paper focuses on two core issues underlying the system performance: the structural design of long-reach manipulators [10–17], and the aerodynamic effects induced by UAV downwash [18–23], both of which have attracted extensive research attention in existing studies.

Recent advances in downward-extended long-arm aerial manipulation aim to increase the vertical separation between the propulsion-induced disturbance region and the physical interaction workspace by mounting the manipulator beneath the UAV. This configuration is intended to improve operational safety, expand the reachable workspace, and enhance accessibility in cluttered or contact-sensitive environments. Compared with rigidly integrated aerial manipulators located near the vehicle body, long-arm configurations offer improved collision avoidance, greater manipulability in vertically constrained scenes, and reduced direct downwash interference during close-proximity operations. Early work primarily considered short-reach arms rigidly attached to multirotor platforms. Kondak et al. [10] demonstrated one of the earliest systems combining a lightweight multi-DOF manipulator with a quadrotor, validating autonomous contact interaction and force-controlled tasks; however, the tight structural coupling between the arm and UAV limited workspace extension and intensified aerodynamic interactions. Franchi et al. [11] subsequently established a unified modeling and control framework for aerial manipulators, systematically analyzing coupled vehicle-manipulator dynamics and interaction stability, and laying the theoretical groundwork for later structural innovations. To further mitigate aerodynamic disturbances while extending operational reach, downward-extended long-arm concepts were progressively introduced. Nekoo et al. [12] proposed a constraint-based optimal design framework for a dual-arm long-reach system comprising a multirotor platform and two lightweight seven-degree-of-freedom manipulators. A structural mass-distribution model and a dynamics-constrained optimization formulation were developed to examine the effects of link length, mass allocation, and joint torque limits on manipulability and flight stability. Although simulations demonstrated task feasibility under thrust and structural constraints, validation remained largely model-based and offline. Suarez et al. [13] further compared standard and long-reach compliant bimanual aerial manipulators and showed that the passive-pendulum long-reach configuration can extend the effective workspace and improve operational safety by increasing the separation between the multirotor and surrounding obstacles. Meanwhile, cable-suspended long-distance aerial manipulation approaches emerged. Sarkisov et al. [14] introduced a winch-equipped multirotor system integrating a dual-cable gripper and an IMU-based swing-suppression mechanism; experiments verified stable oscillation attenuation for suspension lengths up to 3 m. Nevertheless, torsional controllability remained limited, grasping precision depended heavily on manual piloting, and longer cables introduced additional dynamic instability. In an application-oriented study, Suarez et al. [15] employed a long-reach aerial manipulator for in-flight device delivery in power-line maintenance and showed, through CFD analysis and indoor experiments, that increasing the vertical separation between cooperating aerial robots can reduce downwash interference and collision risk. To improve safety in contact-rich tasks, compliant and variable-stiffness long-arm designs were explored. Jalali et al. [16] presented a lightweight compliant long-arm aerial manipulator to enhance disturbance tolerance and interaction robustness; however, compliance inherently reduces end-effector stiffness and can constrain high-precision manipulation. Addressing this trade-off, Fernandez et al. [17] developed a long-range aerial manipulation platform incorporating a variable-stiffness link

(VSL), demonstrating improved disturbance isolation in flexible mode and enhanced accuracy in rigid mode. However, stiffness switching required approximately 7.8 s, limiting dynamic responsiveness, and performance gains were reduced under heavy payload conditions.

More recent studies have emphasized structural efficiency optimization and aerodynamic compatibility while extensively investigating the aerodynamic characteristics of rotor-induced downwash using both numerical simulations and experimental measurements. Liu et al. numerically analyzed aerodynamic interference in multirotor configurations using CFD and demonstrated that the near-wake region beneath the rotor disk exhibits pronounced velocity gradients and strong aerodynamic interactions among rotor wakes [18]. Dougherty et al. [19] further numerically examined the effects of p-ropeller separation and onset-flow conditions on quadcopter propellers, showing that rotor interaction depends jointly on propeller spacing, wake interaction, and incoming-flow conditions, and that onset-flow velocity can noticeably alter propeller performance. Tang et al. systematically simulated the spatial evolution of multirotor downwash and reported that the rotor wake develops through vortex-ring formation and turbulent wake expansion, while the induced velocity gradually attenuates as the flow propagates downstream [20]. Furthermore, Chen et al. conducted high-resolution numerical simulations and revealed that the evolution and diffusion of blade-tip vortices dominate the near-field wake dynamics, thereby determining the overall flow structure beneath the rotor disk [21]. To further validate these numerical predictions, Jin et al. compared CFD simulations with lidar-based measurements and demonstrated that rotor-induced flows exhibit a pronounced axial downwash core together with rapidly decaying radial velocity components in the surrounding flow field [22]. Using a controlled experimental setup, Flem et al. [23] mapped the propeller-induced flow below a multi-rotor UAV with a mobile array of sonic anemometers and showed that the disturbance decreases rapidly away from the downwash centerline, while the individual rotor cores merge into a single downwash region several rotor diameters beneath the rotor plane. De Gregorio et al. experimentally characterized the wake structure of hovering rotors using particle image velocimetry (PIV) and quantitatively confirmed the presence of helical tip vortices together with progressive wake diffusion during downstream propagation [24]. In addition, Gajo et al. performed combined numerical and experimental analyses and demonstrated that rotor wakes exhibit strongly anisotropic decay characteristics, with radial diffusion occurring significantly faster than axial velocity attenuation [25]. Beyond free-flight hovering conditions, Liu et al. [26] analyzed the coupled ground-sidewall interference acting on a small-scale propeller and found that confined boundaries can induce strong force fluctuations and pronounced aerodynamic perturbations, with the strongest coupling effects occurring near a height of approximately 1R.

These findings collectively indicate that rotor downwash contains a high-momentum axial core and exhibits direction-dependent decay behavior. Consequently, manipulators operating directly beneath the rotor disk may experience significant aerodynamic disturbances, whereas laterally extending the manipulator away from the rotor axis can effectively exploit the faster radial decay of the wake to reduce aerodynamic interference and improve operational stability. At the airframe level, Morishita et al. [27] proposed an H-shaped variable-rotor drone capable of creating a windless zone directly beneath the platform and showed that increasing rotor angle redistributes the downwash outward, thereby weakening the flow directly under the UAV. Building on this concept, Miyahara et al. [28] developed and flight-verified a downwash-reducing UAV equipped with adaptive rotors, demonstrating that rotor tilting can markedly suppress the downward airflow while maintaining stable hovering performance in both indoor and outdoor tests.

The aforementioned findings provide a clear physical insight into the mechanism: the near-field rotor downwash is spatially nonuniform, with a dominant axial high-momentum

core and rapidly decaying lateral components. As a result, any target located directly beneath the rotor disk is continuously exposed to strong vertical airflow, which can induce oscillations, deformation, or unintended detachment of lightweight, compliant, or aerodynamically sensitive objects. From a system-design perspective, this defines a significant aerodynamic constraint, making the vertical projection of the rotor disk a high-disturbance zone that should be carefully accounted for when allocating task space and configuring aerial arms.

Therefore, these anisotropic attenuation characteristics should be fully taken into account in the design of long-reach aerial manipulators, extending the workspace laterally to operate outside the axial high-momentum core. This lateral extension, however, would inevitably result in such challenges as mass redistribution, increased structural moment of the arm, and amplified dynamic coupling with the underactuated UAV platform. From the control perspective, Sumathy et al. [29] developed a quadcopter manipulator system with an extended workspace above and below the airframe and proposed a robust adaptive control framework to compensate for coupling effects and external disturbances during manipulator motion. At the task-execution level, Zhang et al. [30] incorporated CFD-derived rotorwash models into motion planning and nonlinear model predictive control, enabling rotorwash-aware grasping by reducing or redirecting aerodynamic disturbance on lightweight targets.

In this work, we propose a physics-guided design and analysis framework for a multirotor-based aerial manipulator intended for high-altitude fruit harvesting or sampling tasks. Unlike conventional approaches that treat aerodynamic disturbances as external uncertainties to be compensated at the control level, the proposed methodology explicitly integrates rotor-induced downwash into the structural configuration process. By modeling the anisotropic attenuation of the near-field flow, the manipulator workspace is spatially reallocated away from the axial high-momentum region, effectively mitigating disturbances through structural layout rather than solely relying on active control. Specifically, link lengths, joint placements, and material distribution are co-optimized to balance lateral extension with overall center-of-gravity distribution, preventing excessive moment amplification and ensuring platform-level stability. Beyond that, flight-attitude stabilization and end-effector motion planning are jointly coordinated to minimize aerodynamic-dynamic coupling during interaction. Combined design of the structure and control strategy helps reduce oscillation amplitudes, lower the probability of grasp failure, and improves task success rates. Moreover, the framework minimizes airflow disturbance to surrounding vegetation, enhancing ecological compatibility and operational safety in natural forest environments.

As such, this work not only provides an application-oriented system implementation but also proposes a transferable structural-aerodynamic co-design principle for aerial robotic platforms handling disturbance-sensitive objects. The remainder of this paper is organized as follows. Section 2 presents the design and manipulation mechanism of an aerial robotic arm. followed by its kinematic modeling and downwash effect analysis of its gripper and targets in Section 3. Section 4 details the construction and experiments of a long-reach aerial manipulator prototype for validating the feasibility of the proposed design methodology. Section 5 discusses the results and concludes this work.

2. Design and Manipulation Mechanism of the Aerial Robotic Arm

2.1. Structural Design

In this section, a 3-DOF aerial manipulator integrated with a six-rotor UAV platform is presented, as illustrated in Figure 1. The aerial arm comprises a control module, three revolute joints actuated by servomotors, two elongated rigid links, and a lightweight end-effector equipped with an additional servo. The UAV platform also integrates navigation

and communication modules, including GPS, RTK, and RF systems. The aim of such structural design is to enable lateral workspace reallocation and stable grasping of elevated targets under rotor-induced aerodynamic disturbances.

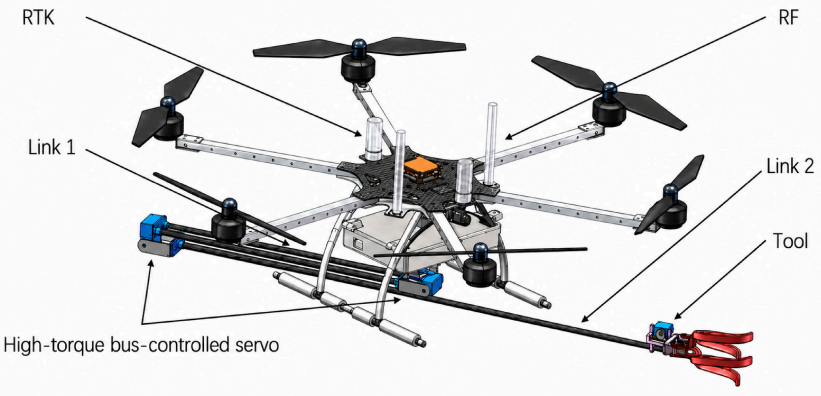

Figure 1. Colored structural configuration and functional layout of the aerial-arm system, showing the UAV platform, control module, revolute joints, elongated links, end-effector, and navigation/communication components.

In previous aerial manipulation studies, the term "long-reach" has generally been used to describe configurations in which the end-effector or manipulation unit is spatially separated from the UAV body by an extended link, flexible connection, or suspended structure, thereby enlarging the effective workspace, improving the safety distance, and reducing collision or downwash-related risks [13,15]. However, no universally accepted quantitative threshold has been established for defining a long-reach aerial manipulator. Therefore, in this study, the long-reach characteristic is defined relative to the characteristic size of the UAV platform and the aerodynamic purpose of downwash avoidance. Specifically, the maximum extended length of the manipulator is 1.20 m, which is approximately 1.5 times the rotor-to-rotor distance of the UAV platform, i.e., 0.80 m. This geometric scale enables the end-effector to be displaced away from the rotor-projected high-momentum downwash core and to operate in a comparatively weak-disturbance region. Accordingly, the term "long-reach" in this paper denotes not only extended geometric reachability but also a downwash-aware spatial separation strategy.

To this end, the manipulator is intentionally configured with extended rigid links to provide sufficient lateral reach, thereby relocating the operational workspace outside the high-momentum axial downwash region beneath the rotor disk. Meanwhile, the use of a minimal number of joints reduces structural complexity and mitigates dynamic coupling between the manipulator and the underactuated aerial platform. This configuration is designed to achieve a balanced trade-off among workspace coverage, aerodynamic safety, and dynamic robustness, with the aim of enabling stable interaction without excessive inertial amplification.

The link dimensions are not arbitrarily selected but are explicitly constrained by the aerodynamic field characteristics associated with rotor-induced downwash. Specifically, these dimensions are determined by quantitatively analyzing the axial velocity concentration zone, lateral attenuation behavior, and the minimum safe operational distance from the high-momentum core region.

2.2. Manipulation Mechanism

To preserve the fidelity of aerodynamic-structural verification while avoiding unnecessary computational burden, a lightweight microcontroller is adopted, thereby reducing system mass, power consumption, and hardware complexity. Rather than relying on

high-performance onboard computation to compensate for disturbances after they occur, the proposed framework assumes that disturbance mitigation should originate from the structural configuration itself. The control-hardware configuration is shown in Figure 2.

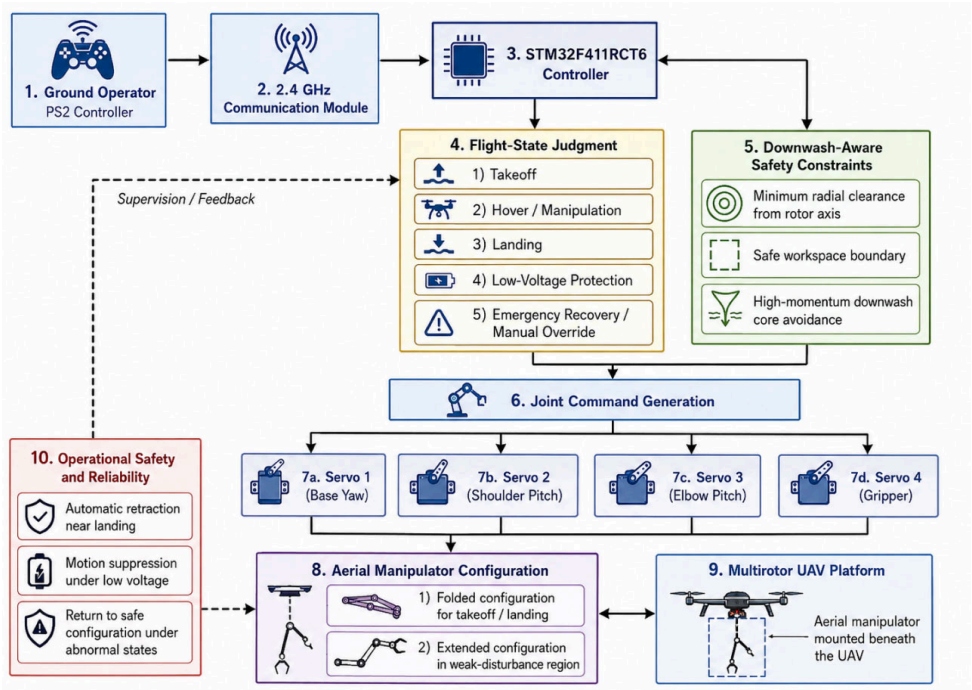

Figure 2. Control logic and hardware implementation of the aerial-arm system.

Manipulator actuation is implemented through manual teleoperation using a PS2 wireless controller (TaKe Innovation, Yantai, China). This approach is intentionally selected to maintain experimental transparency and preserve the interpretability of operator commands during validation trials. At the core of the embedded system, an STM32F411RCT6-based control board (Zhengdian Atom, Guangzhou, China) performs joint-level control, enforces safety constraints, and processes motion commands within a deterministic, low-latency environment. Although computational resources are intentionally constrained, the platform provides sufficient real-time capability to ensure stable manipulation without introducing excessive algorithmic complexity. This balance between capability and restraint is critical for assessing whether structural disturbance avoidance alone can sustain safe aerial manipulation.

Safety considerations extend beyond mechanical integrity to encompass aerodynamic awareness. Rotor-induced downwash, characterized by a high-momentum axial core and radial attenuation, forms a disturbance field that directly influences manipulator operation. To prevent unintended interaction with this core region, a minimum radial clearance from the rotor axis is enforced in real time. Joint trajectories that approach the high-momentum zone are automatically restricted, translating knowledge of the downwash distribution into executable geometric constraints. In this manner, airflow characteristics are treated as spatial boundaries embedded within the control framework.

The revised control logic consists of manual teleoperation input, wireless communication, embedded controller processing, flight-stage judgment, joint-command generation, and downwash-avoidance constraint execution. Commands from the PS2 wireless controller are first transmitted to the STM32F411RCT6-based control board through the 2.4 GHz communication module. The controller then generates corresponding joint commands according to the current operation state, including takeoff, hovering, manipulation, retraction, landing, low-voltage protection, and emergency recovery. During manipulation, the

controller also checks whether the end-effector approaches the high-momentum downwash region and constrains the joint motion within the safe workspace through joint-angle limits.

Operational resilience is further enhanced through mode-dependent behaviors embedded in the control logic. During takeoff, when aerodynamic sensitivity is most pronounced, the manipulator remains folded to minimize flow interaction by reducing the exposed aerodynamic area and avoiding intrusion into the high-velocity axial downwash core. As landing approaches and attitude margins narrow, automatic retraction helps preserve vehicle balance. Under degraded power conditions, low-voltage protection suppresses large-amplitude motions to prevent abrupt energy depletion, while an emergency recovery routine commands an immediate return to a predefined safe configuration whenever abnormal flight states or manual overrides are detected. Each mechanism addresses a specific flight-phase vulnerability, contributing to improved overall system reliability.

Generally, the control architecture reflects a deliberate integration of lightweight embedded computation with structurally informed aerodynamic safeguards. By embedding workspace boundaries and disturbance-aware geometric constraints directly into the joint-level control loop, the system simultaneously regulates aerodynamic clearance, structural stability, and operational safety—without resorting to computationally intensive active disturbance-rejection strategies. This resource-efficient yet physically grounded framework is particularly well suited to prototype validation and early-stage development of disturbance-aware aerial manipulation systems, where clarity of experimental interpretation is as critical as performance itself.

3. Modeling and Analysis

3.1. Kinematic Modeling

Figure 3 illustrates the reference frames, position vectors, joint variables, link-length parameters, and height-constraint plane of the developed 3-D manipulator. Subscripts of E, B and 0 denote the Earth-fixed coordinate system, UAV-fixed coordinate system and the manipulator base coordinate system, respectively. The revised schematic explicitly marks the base coordinate frame, three revolute joint variables, two link lengths, TCP position, and the base mounting plane, below which the manipulator must remain during folded takeoff and landing configurations.

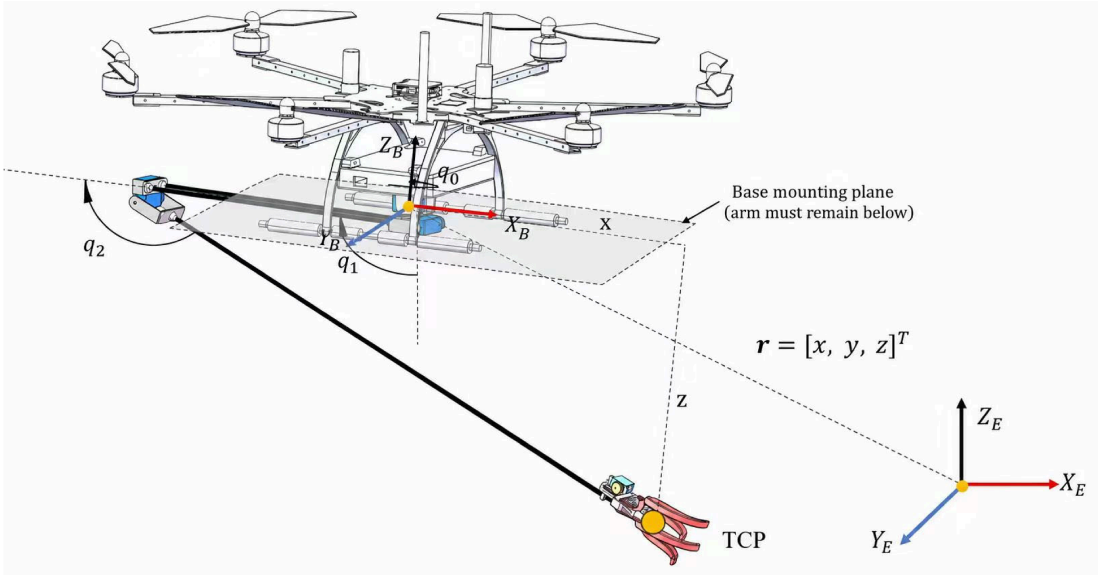

Figure 3. Kinematic schematic of the 3-DOF aerial manipulator with joint variables, link lengths, TCP, and height-constraint plane.

The UAV platform's position is defined by the vector of $\boldsymbol{r}$ in the coordinate system of $OX_EY_EZ_E$, that is,

$$\boldsymbol{r} = \left[x_0,\ y_0,\ z_0\right]^T \tag{1}$$

where x_0, y_0, and z_0 denote the platform position components in the Earth-fixed frame, respectively. The manipulator is a 3-D serial RRR structure, and its joint variables include:

q_0: base yaw angle of Servo 1, [0, 2π].

q_1: shoulder pitch angle of Servo 2, $[-\pi, 0]$.

q_2: elbow pitch angle of Servo 3, $[-\pi, 0]$.

The lengths of the manipulator's links are defined as:

L_1: length of Link 1.

L_2: length of Link 2.

The three-dimensional workspace is obtained by rotating the planar section about the vertical axis; therefore, the planar workspace should be analyzed first. The base joint, or Servo 1, is located at the origin of the coordinate system. When the y-coordinate of the TCP is 0, in this condition, the x- and y- coordinates of the TCP in $OX_BY_BZ_B$

$$x = L_1\cos\, q_1 + L_2\cos\,(q_1 + q_2) \tag{2}$$

$$z = L_1\sin\, q_1 + L_2\sin\,(q_1 + q_2) \tag{3}$$

To facilitate compact folding, reduce power consumption during non-operational phases, and improve the stability of the aerial-manipulation system during takeoff and landing, the link-length ratio was selected such that the manipulator center of mass remains close to the UAV center of gravity in the folded configuration. As such, $L_1 = L$, and $L_2 = 2L$ are assumed. We have

$$x = L\cos\, q_1 + 2L\cos\,(q_1 + q_2) \tag{4}$$

$$z = L\sin\, q_1 + 2L\sin\,(q_1 + q_2) \tag{5}$$

which describes the planar reachable region.

To ensure physically realizable motion, the allowable ranges of the three joints were first defined as follows. For flight safety, no link may rise above the first joint plane. The manipulator must remain below the fuselage. As such, we introduce a new constraint of

$$q_1 + q_2 \in [-\pi, 0] \tag{6}$$

Thus, $z \leq 0$, which distinguishes the present workspace from that of a conventional planar 2R mechanism.

Based on the above joint constraints, the outer boundary of the planar reachable workspace can be derived from the fully extended manipulator configuration. When the arm is fully extended, that is, $q_2 = 0$, coordinates of the end-effector can be rewritten as

$$x = 3L\cos\, q_1 \tag{7}$$

$$= 3L\sin\, q_1 \tag{8}$$

Eliminating q_1 yields

$$x^2 + z^2 = 9L^2 \tag{9}$$

Considering $q_1 \in [-\pi, 0]$, the outer boundary is the lower semicircle of radius $3L$. In addition to the maximum reach, the folded-link configuration also gives rise to an inner boundary that defines the inaccessible region near the base. Due to the height constraint,

the arm cannot fully fold upward. The inner boundary occurs when the second link is horizontal, that is,

$$q_1 + q_2 = 0 \tag{10}$$

Substituting Equation (10) into Equations (7) and (8), we obtain

$$x = L\cos q_1 + 2L \tag{11}$$

$$z = L\sin q_1 \tag{12}$$

Combining Equations (11) and (12), we have

$$\left(x - 2L\right)^2 + z^2 = L^2 \tag{13}$$

This is a circle region centered at $[2L, 0]$ with a radius of L. Only the lower half satisfies $z \leq 0$.

By combining the outer and inner boundaries, the effective planar reachable domain of the manipulator can be determined. The planar workspace is

$$\Omega_2 = \left\{(x, z) \mid z \leq 0,\ x^2 + z^2 \leq 9L^2, \left(x - 2L\right)^2 + z^2 \geq L^2\right\} \tag{14}$$

Geometrically, this region is a lower semicircle with an eccentric inner exclusion zone.

On this basis, the corresponding workspace area can be obtained by integrating the admissible planar domain. Outer semicircle:

$$A_{outer} = \frac{9}{2}\pi L^2 \tag{15}$$

Inner semicircle:

$$A_{inner} = \frac{1}{2}\pi L^2 \tag{16}$$

Planar workspace area:

$$A = 4\pi L^2 \tag{17}$$

From a physical perspective, these geometric results clarify how the link dimensions and joint limits jointly determine the effective operating range of the manipulator. The workspace exhibits the following characteristics: Maximum horizontal and vertical reach equals; A central unreachable region exists; The geometry forms an eccentric annular half-domain; All reachable points lie below the base plane. The eccentric inner boundary arises from flight safety constraints. This feature distinguishes aerial arms from conventional planar mechanisms. Given that ranges from 0 to 2π, then the actual workspace of the TCP should be an eccentric hemispherical domain, as shown in Figure 4.

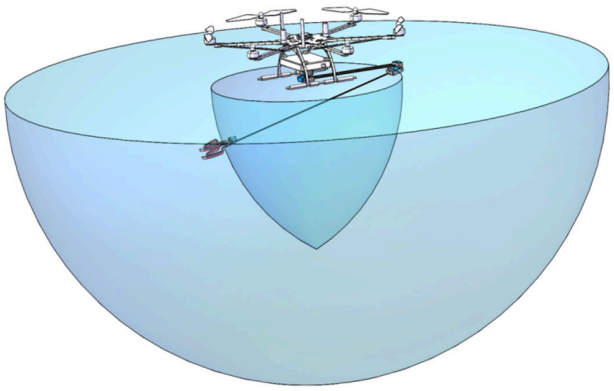

Figure 4. Geometric analysis of the planar reachable workspace.

3.2. Downwash Effects on the Gripper and Targets

To quantitatively characterize the aerodynamic environment generated by the multirotor platform, a three-dimensional computational fluid dynamics (CFD) analysis was conducted to resolve the rotor-induced flow field and its spatial evolution. The simulation aims to reveal the wake structure and velocity distribution beneath the rotor system, which directly influence the operating region of the aerial manipulator.

To improve computational efficiency while preserving the essential aerodynamic characteristics of the UAV, the geometric model of the multirotor platform was first simplified prior to numerical simulation, as illustrated in Figure 5. The simplification of the UAV geometry was not arbitrary, but was established based on an aerodynamic feature-retention principle commonly used in UAV and rotor CFD studies [31–34]. Previous studies have shown that rotor modeling methods, rotor-airframe aerodynamic interference, and wake-structure prediction are key factors in the numerical simulation of multirotor UAV flows. Therefore, the present CFD model focuses on the large-scale spatial distribution of the rotor-induced downwash and its influence on the manipulator workspace. The rotor disks, supporting arms, and central fuselage were retained because they directly affect the formation and evolution of the rotor wake. In contrast, secondary structures, such as the landing gear, sensor mounts, and small auxiliary components, were omitted or replaced by simplified geometric representations, since their influence on the overall downwash distribution is relatively limited while their detailed inclusion would substantially increase local mesh density and computational cost. This simplification strategy reduces computational complexity while retaining the dominant wake-prediction capability required for the present downwash-aware workspace analysis.

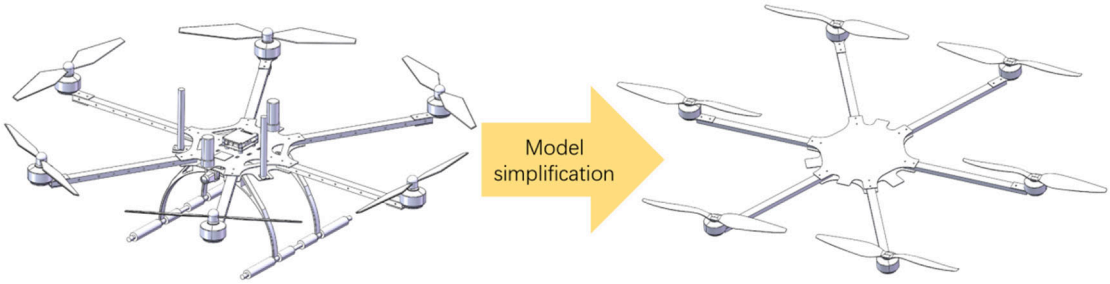

Figure 5. Simplified UAV geometry for numerical simulation.

Based on the simplified geometric model, the corresponding numerical solution framework was further established to resolve the rotor-induced flow field. All simulations were performed using the finite-volume solver ANSYS Fluent 2025 R1. The governing equations were the incompressible Reynolds-averaged Navier-Stokes (RANS) equations for turbulent viscous flows. Pressure-velocity coupling was handled using the SIMPLE algorithm, and second-order upwind discretization schemes were employed for the convective terms to improve numerical accuracy. The shear-stress-transport (SST) turbulence model was adopted to capture wake development and shear-layer dynamics in the rotor-induced flow field. The convergence criterion for all residuals was set to 1×10^{-5}.

Based on the above numerical settings, the computational domain and mesh system were further configured to ensure accurate resolution of wake evolution while minimizing boundary-induced effects. The computational domain was defined with respect to the rotor plane, where D denotes the rotor diameter. To reduce the influence of boundary conditions on wake development, the domain was extended approximately 10D upstream of the rotor plane, 10D in the radial direction, and 15D downstream of the rotor plane. This domain size covers the rotor near-wake, wake-merging region, and downwash attenuation

region, thereby providing a sufficient computational space for the subsequent aerodynamic workspace-constraint analysis. A hybrid mesh strategy was adopted, with local refinement applied near the rotor disks and in the initial wake region to capture the strong velocity gradients and wake structures induced by the rotating blades, while a relatively coarser unstructured mesh was used in the far-field region to reduce computational cost. The final mesh contained approximately 3.2 million cells. No full grid-independence analysis is claimed in the present revision because additional calculations with multiple mesh densities were not conducted. Instead, the CFD setup is reported with detailed mesh, boundary conditions, operating conditions, and convergence information, and the numerical results are further compared with experimental airflow measurements for validation.

The main numerical parameters, including the governing equations, turbulence model, computational domain, mesh strategy, rotor-motion modeling method, boundary conditions, and residual convergence criterion, are summarized in Table 1.

Table 1. Key numerical settings of the CFD model.

Item	Setting
Software	ANSYS Fluent 2025 R1
Governing equations	Incompressible RANS equations
Turbulence model	SST model
Pressure-velocity coupling	SIMPLE algorithm
Spatial discretization	Second-order upwind scheme
Rotor modeling	Multiple reference frame (MRF) approach
Rotating domain	An individual rotating fluid domain was assigned to each rotor
Rotor angular velocity	600 rad/s, corresponding to approximately 5729 rpm under hovering condition
Computational domain	10D upstream, 10D radial, and 15D downstream of the rotor plane
Mesh strategy	Hybrid mesh with local refinement near the rotor disks and initial wake region
Total cell number	Approximately 3.2 million cells
Boundary conditions	Pressure inlet at the upper boundary; pressure outlet at the lower boundary; wall boundaries at the lateral sides; no-slip wall conditions for the UAV body, supporting arms, and rotor surfaces
Ground effect	No ground wall was included in the computational domain
Convergence criterion	Residuals below 1×10^{-5}

The computational domain was divided into rotating and stationary fluid regions. Each rotor was enclosed by an individual rotating fluid domain and modeled using the multiple reference frame (MRF) approach, while the surrounding flow field was treated as a stationary fluid region [31]. The angular velocity of each rotating domain was set to 600 rad/s, corresponding to approximately 5729 rpm under the hovering condition. The upper boundary of the computational domain was defined as a pressure inlet, and the lower boundary was defined as a pressure outlet. The lateral boundaries were set as walls; however, the radial size of the computational domain was extended to approximately 10D to reduce the influence of lateral confinement on the main downwash region. No-slip wall boundary conditions were applied to the UAV body, supporting arms, and rotor surfaces. No ground wall was included in the computational domain, so the simulation represented rotor-induced downwash in an open-space hovering condition without ground effect.

As illustrated in Figure 6, eight horizontal sampling planes were arranged beneath the UAV at equal vertical intervals of 0.25D, where D is the rotor diameter. The corresponding vertical velocity contours on these planes are shown in Figure 7a–h, which quantitatively

reveal the spatial evolution of the downwash field beneath the rotor system. In the sections closest to the rotor plane [Figure 7a,b], the strongest downwash remains concentrated beneath the individual rotor disks, and the local peak velocity reaches approximately 8–10 m/s according to the color scale. At this stage, the high-velocity zones are still mainly separated from one another, indicating that the individual rotor wakes have not yet fully merged immediately below the UAV. As the distance below the vehicle increases [Figure 7c,d], the initially separated wakes begin to interact beneath the fuselage and form a more coupled flow structure. Although the strongest high-velocity regions shrink compared with the nearest sections, multiple concentrated streaks are still clearly visible, with representative values remaining on the order of 6–8 m/s. Further downstream [Figure 7e,f], the high-speed region contracts significantly, and the overall velocity level decreases to approximately 2–4 m/s. In the farthest sections [Figure 7g,h], most of the flow field has decayed to below about 1–2 m/s, indicating that the downwash has gradually transitioned from a strong-disturbance regime to a weak-disturbance regime. These results show that the downwash beneath the UAV has a finite axial persistence, while its intensity decreases markedly after the wake-merging region.

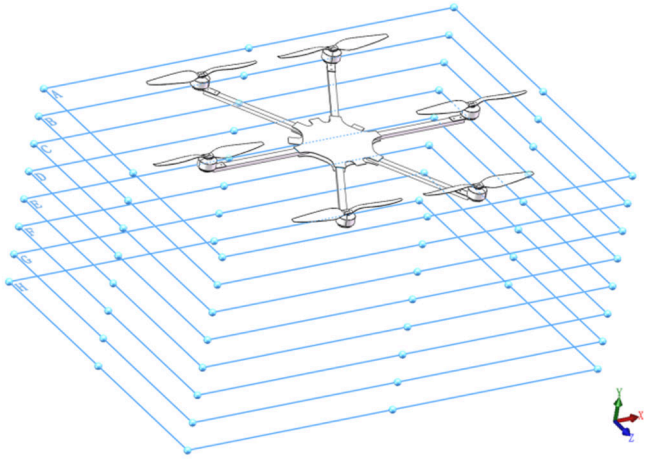

Figure 6. Spatial arrangement of the eight horizontal sampling planes beneath the UAV. Adjacent planes are spaced at equal vertical intervals of 0.25D, where D is the rotor diameter.

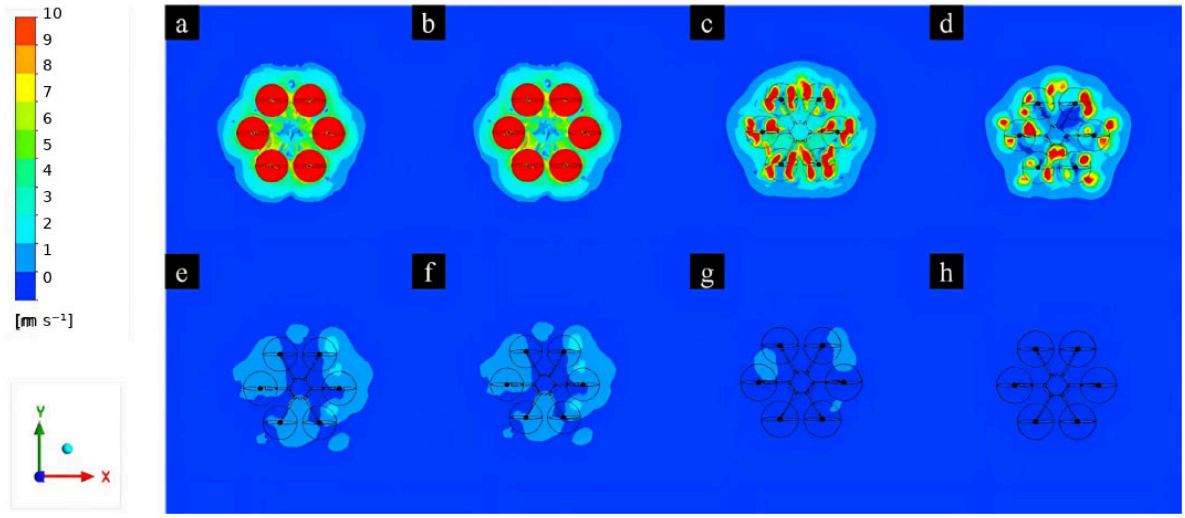

Figure 7. Vertical velocity contours of the downwash flow on the eight horizontal sections beneath the UAV. Panels (**a**–**h**) correspond to the sampling planes in Figure 6 in sequence, at equal vertical intervals of 0.25D, showing the evolution and attenuation of the downwash core below the rotor.

Another important feature evident from Figure 7a–h is the strong spatial localization of the downwash core. At all section levels, the highest velocities remain confined to a limited area near the rotor-projected region, whereas the surrounding flow rapidly transitions from the red/yellow high-speed band to the cyan/blue low-speed band over a comparatively short lateral distance. This indicates that the strong-disturbance zone is not uniformly distributed beneath the entire fuselage, but instead occupies a bounded high-momentum region with relatively rapid attenuation outside the wake core.

The centerline velocity profile shown in Figure 8 further quantifies the vertical evolution of the downwash directly beneath the UAV. Along the vertical centerline, the induced velocity first increases from approximately 2.5 m/s to a local maximum of about 4.3 m/s in the near-wake region, and then decreases rapidly to below 1 m/s after several sampling intervals, eventually approaching zero in the far field. This non-monotonic variation indicates that the wakes generated by the individual rotors converge and intensify beneath the fuselage before gradually dissipating downstream. Therefore, the region directly beneath the UAV cannot be regarded as a uniformly disturbed zone; rather, it contains a spatially bounded high-momentum core, and this anisotropic flow structure constitutes the key aerodynamic constraint governing the manipulator layout.

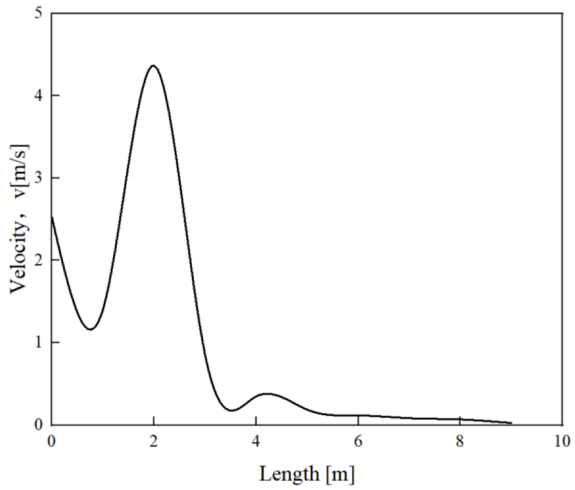

Figure 8. Variation in the vertical downwash velocity along the vertical centerline directly beneath the UAV. The results quantify the attenuation of the induced velocity with increasing distance from the rotor plane.

The flow characteristics in front of the UAV were further evaluated using the eight vertical sampling planes shown in Figure 9, which were arranged ahead of the vehicle at equal forward intervals of 0.25D. The corresponding velocity contours are presented in Figure 10a–h. Compared with the downwash field beneath the UAV shown in Figure 7a–h, the induced flow in the forward region is markedly weaker and spatially milder. In the planes closest to the UAV [Figure 10a,b], localized accelerated flow still appears near the rotor level, but the affected area remains limited, and no continuous high-momentum core comparable to that beneath the fuselage is observed. As the forward distance increases [Figure 10c–h], the induced-flow intensity decreases progressively, and the remaining high-velocity regions shrink rapidly to isolated weak-disturbance zones. This trend is further quantified by the centerline profile in Figure 11. Along the forward centerline directly ahead of the UAV, the induced velocity decreases monotonically with increasing forward distance, dropping from about 3.0 m/s near the vehicle to below 1.0 m/s after several sampling intervals, and then continuing to decay toward zero in the far field. These results indicate that rotor-induced acceleration is predominantly concentrated in the downward direction rather than in the forward direction. Therefore, from the viewpoint of

aerodynamic interference, the region directly beneath the fuselage constitutes the dominant exclusion zone, whereas the forward and laterally offset regions provide a comparatively more stable aerodynamic environment for manipulation.

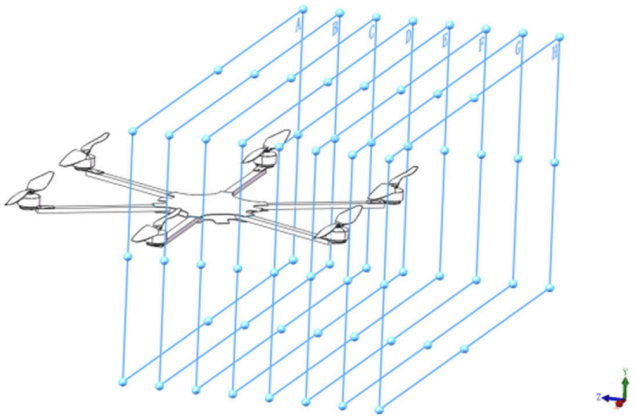

Figure 9. Spatial arrangement of the eight vertical sampling planes ahead of the UAV. Adjacent planes are spaced at equal forward intervals of 0.25D, where D is the rotor diameter.

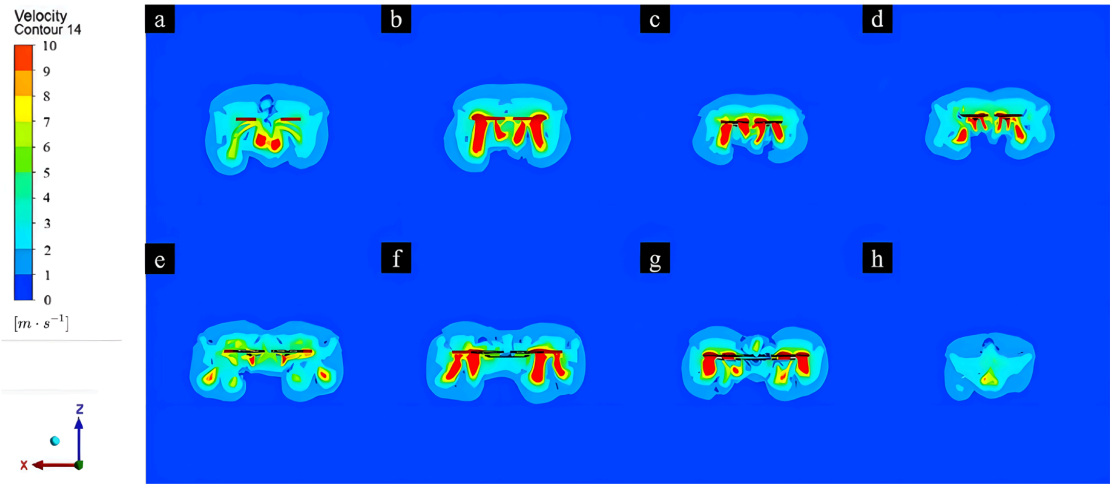

Figure 10. Induced-flow velocity contours on the eight vertical sampling planes ahead of the UAV. Panels (**a**–**h**) correspond one-to-one to the planes shown in Figure 9, with adjacent sections separated by 0.25D. The results illustrate the spatial evolution and attenuation of the induced flow in the region ahead of the UAV.

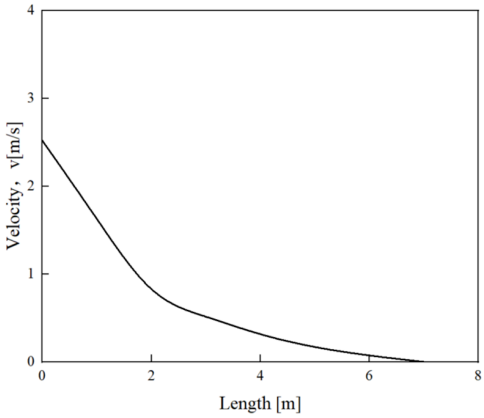

Figure 11. Variation in the induced-flow velocity along the forward centerline directly ahead of the UAV. The results quantify the attenuation of the induced velocity with increasing forward distance from the UAV.

The above quantitative observations directly explain why the manipulator links cannot be designed solely according to geometric reachability. If the end-effector remains within the high-momentum wake core beneath the UAV, it will be continuously exposed to induced velocities of several meters per second, which can destabilize grasping, increase target disturbance, and amplify structural oscillation of the long-reach arm. In contrast, once the end-effector is displaced away from the rotor-projected wake core toward the forward or laterally offset region, the induced velocity decreases significantly, and the aerodynamic environment becomes much more favorable for stable operation. Therefore, the manipulator must provide sufficient horizontal and forward offset capability to relocate the end-effector outside the strong downwash core, rather than merely extending downward [35–37]. This aerodynamic requirement directly explains why a long-reach manipulator configuration is necessary.

Compared with the region beneath the UAV, the induced velocity ahead of the rotor system is significantly weaker. This phenomenon can be attributed to the fact that the rotor thrust primarily accelerates the airflow downward rather than forward. Consequently, the aerodynamic disturbance in the upstream region of the UAV remains relatively limited.

The velocity contours show only mild variations in the flow field ahead of the UAV. These results suggest that the aerodynamic interference generated by the rotor system is predominantly confined to the region beneath the vehicle. Therefore, the forward region of the UAV provides a comparatively stable aerodynamic environment.

3.3. Experimental Setup and Validation

To further validate the reliability of the CFD results, a controlled experimental setup was established, as illustrated schematically in Figure 12, and representative physical setups are shown in Figure 13. In both measurement scenarios, the UAV was laterally fixed on a rigid support frame to eliminate flight-induced motion and ensure repeatable measurement conditions.

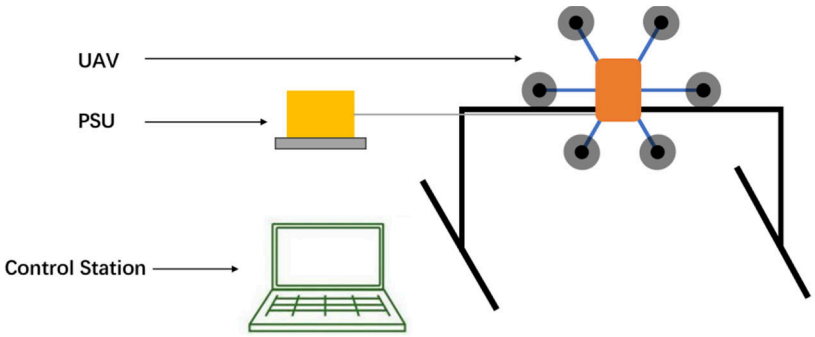

Figure 12. Schematic of the experimental setup for downwash velocity measurement.



Figure 13. Experimental setup for airflow velocity measurement of underside and side of the UAV.

The UAV was laterally fixed on a rigid support frame to eliminate flight-induced motion and ensure repeatable measurement conditions. The installation height and surrounding clearance were carefully designed such that the UAV was positioned sufficiently far from the ground and nearby walls. This configuration effectively minimizes the influence of ground effect and wall-induced aerodynamic interference. During the fixed-platform airflow measurement, temporary ballast was placed at the base of the support frame only to improve its static stability under rotor-induced airflow. The ballast was located away from the predefined airflow sampling points and was not involved in the measurement procedure. Therefore, its influence on the measured velocity profiles at the selected sampling locations was considered negligible. In future experiments, a more integrated rigid support structure or ground-mounted fixture will be adopted to improve the engineering standardization and repeatability of the experimental setup.

During the experiment shown in Supplementary Video S1, the rotor system was operated at a constant rotational speed corresponding to a hovering condition. Airflow velocity measurements were conducted using a calibrated PM6252A anemometer (Huayi Instrument, Guilin, China), with a measurement range of 0.80–30.0 m/s, an accuracy specified by the manufacturer as ±(2.0% + 50), and a sampling interval of 0.4 s. Specifically, six measurement points were arranged directly beneath the UAV along the vertical axis, and an additional two points were positioned in front of the UAV along the longitudinal direction. This measurement configuration enables a direct comparison between experimental data and CFD results for both axial and forward flow regions. The measured velocity distributions exhibit trends consistent with the numerical predictions. In the region directly beneath the UAV, the airflow velocity reaches its maximum near the rotor plane and decreases progressively with increasing vertical distance. In contrast, the velocity magnitude in the forward direction remains significantly lower and shows a relatively mild variation. Furthermore, the experimental data confirm that the lateral attenuation of velocity is more rapid than the axial decay, demonstrating the anisotropic characteristics of the rotor-induced flow. Figure 14 presents a quantitative comparison between the CFD-predicted velocity profiles and the experimentally measured data, which show a good agreement. It is worth noting that the velocity variations are plotted as a function of distance for both the vertical region beneath the UAV and the forward region ahead of the platform.

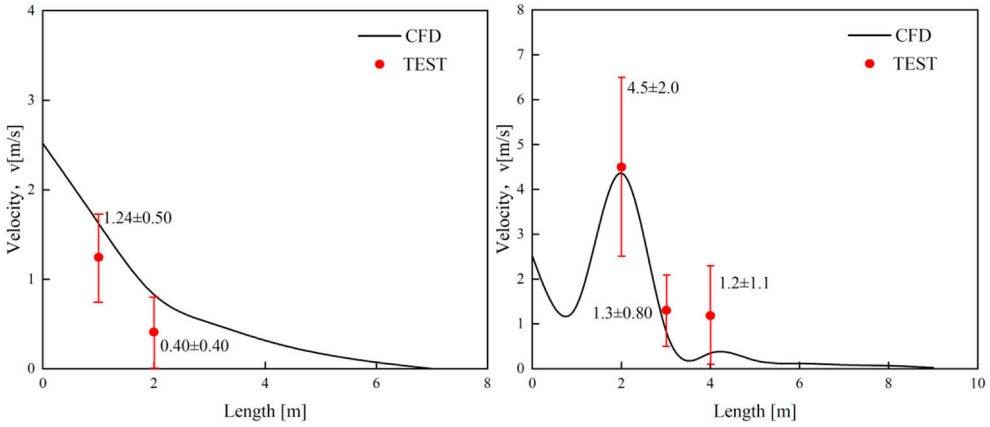

Figure 14. Comparison between experimentally measured and CFD-predicted velocity profiles in the beneath-UAV and forward regions. The red curve and bounds denote the experimental mean and fluctuation range, respectively.

For both the beneath-UAV and forward-region measurements, the CFD-predicted velocity profiles remain close to the experimentally obtained mean values and, at all sampled locations, fall within the corresponding upper and lower fluctuation bounds

marked in red. This result indicates that the numerical model not only captures the overall attenuation trend of the rotor-induced flow, but also reproduces the experimental variation range with satisfactory accuracy. In the region beneath the UAV, the velocity decreases monotonically with increasing vertical distance, and the CFD curve remains consistently near the mean experimental profile. In the forward region, the velocity level is markedly lower and the gradient is milder, and the corresponding CFD prediction likewise stays within the experimental fluctuation envelope. Minor deviations between the numerical and experimental results are still present at some locations, which can be attributed to ambient airflow disturbances, measurement uncertainty, and slight variations in rotor operating conditions. Nevertheless, the overall agreement remains satisfactory, indicating that the present CFD model provides a reliable basis for characterizing the spatial distribution and attenuation behavior of the rotor-induced flow field. This agreement further supports the use of CFD-based flow-field analysis as a dependable foundation for disturbance-aware aerial manipulator design.

3.4. Manipulator Workspace Under Downwash Constraints

The aerodynamic characteristics of the rotor downwash have direct implications for the operational workspace of the aerial manipulator. In particular, the strong velocity core beneath the rotor axis represents a region of significant aerodynamic disturbance. When the manipulator operating region and the target object fall within the strong downwash region, intensified aerodynamic disturbances may introduce additional loads and reduce the overall system stability. Moreover, the stability of the target object during grasping may deteriorate, thereby increasing the difficulty of the aerial manipulation task. To mitigate these effects, an additional downwash-avoidance constraint was incorporated into the workspace analysis. Based on the CFD results, regions characterized by strong downwash velocities were excluded from the feasible workspace of the manipulator. Figure 15 illustrates the resulting reachable workspace after applying the downwash-avoidance constraint.

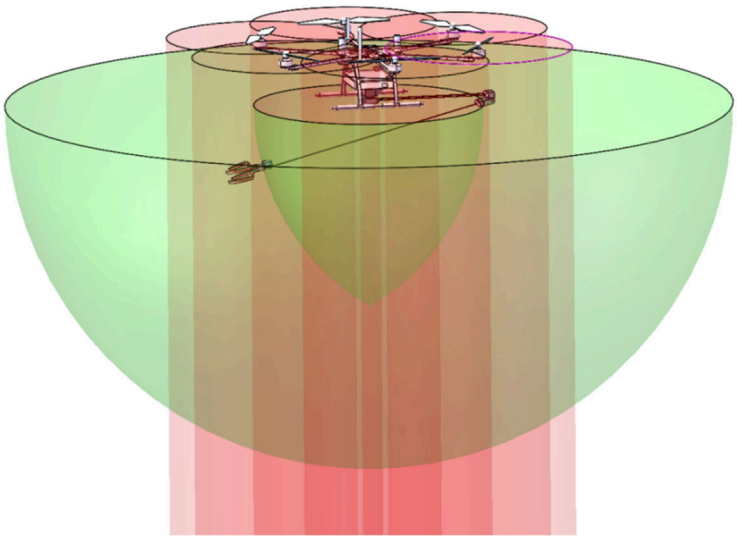

Figure 15. Reachable workspace with an additional downwash-avoidance constraint.

Compared with the unconstrained workspace, the feasible operating region shifts away from the rotor wake core. This result demonstrates that aerodynamic considerations play an important role in the design and deployment of aerial manipulators. By integrating the aerodynamic characteristics of the rotor wake into the workspace analysis, the manipulator can be operated in regions with reduced aerodynamic disturbances. This design strategy improves operational stability and enhances the safety of aerial manipulation tasks.

For this reason, the link dimensions were selected by jointly considering the quantified wake-core extent, the lateral attenuation behavior of the downwash, and the minimum safe operating distance required for end-effector stability. The first link length was constrained to 0.35–0.45 m and the second link length to 0.70–0.90 m, such that the end-effector could be transferred from the high-disturbance zone beneath the UAV to a low-disturbance operating region while still maintaining adequate workspace coverage. After further balancing aerodynamic safety, structural mass, inertia, and platform attitude stability, the final link lengths were chosen as l_1 = 0.40 m and l_2 = 0.80 m. In this sense, the long-reach configuration is not a purely geometric design choice, but a direct consequence of the quantitatively identified rotor-wake distribution.

Based on the CFD-derived downwash-velocity distribution and the selected link parameters, the effective workspace was subsequently redefined. The simulations delineated the spatial extent of the strong downwash core as well as its vertical and lateral decay behavior, which together were used to define an aerodynamically constrained exclusion zone. By superimposing this exclusion zone onto the theoretically derived kinematic workspace and applying a spatial trimming procedure, dynamically unfavorable regions were removed. The resulting workspace not only satisfies kinematic reachability but also ensures that the end-effector operates within low-disturbance flow regions. Compared with a purely geometric definition, this refined workspace explicitly incorporates the coupled constraints imposed by rotor-induced flow and manipulator geometry, thereby providing a more realistic representation of the aerial arm's operational envelope during flight.

4. Construction and Experiments

Building upon the aerodynamic simulation outcomes and the refined workspace evaluation, a long-reach aerial manipulator prototype was developed to experimentally validate the proposed design methodology. The transition from numerical analysis to physical implementation enables direct assessment of whether the disturbance-aware configuration performs as intended under real flight conditions. The fully integrated aerial arm mounted on the UAV platform is shown in Figure 16, and the corresponding structural parameters are summarized in Table 2. These specifications reflect the geometric and mass properties derived from the preceding aerodynamic and kinematic constraints, thereby establishing a consistent linkage between simulation-guided design and hardware realization.

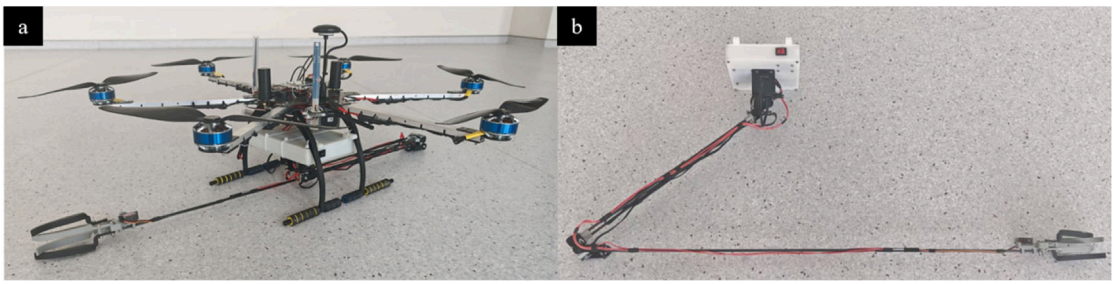

Figure 16. Prototype of the long-reach aerial arm system: (**a**) aerial arm integrated with the UAV; (**b**) aerial arm with the control box.

The aerial platform is a hex-rotor system developed by Nanjing University and integrated with the Mission Planner flight-control framework. It provides reliable attitude stabilization and sufficient payload capacity to maintain flight stability even when the manipulator is fully extended. This capability is essential for evaluating the coupled aerodynamic-structural effects introduced by long-reach aerial manipulation. The embedded control unit of the aerial arm was implemented using an STM32F411RCT6-based

control board (Zhengdian Atom, Guangzhou, China), and manual command input was provided through a PS2 wireless controller (TaKe Innovation, Yantai, China).

Table 2. Technical specifications of the long-reach aerial arm.

Category	Parameter	Unit	Value
Aerial platform	Total weight	kg	3.5
Aerial platform	Maximum payload	kg	2.0
Aerial platform	Endurance time (unloaded)	min	≈25
Aerial platform	Battery pack	-	6S, 8000 mAh, 1.08 kg
Aerial platform	Rotor size	inch	13 × 6
Aerial platform	Rotor-to-rotor distance	mm	800
Aerial platform	GPS	-	Included
Aerial platform	RTK	-	Included
Long-reach aerial arm	Servo 1 rotation range	°	270
Long-reach aerial arm	Servo 1 stall torque	kg·cm	25
Long-reach aerial arm	Servo 2 rotation range	°	180
Long-reach aerial arm	Servo 2 stall torque	kg·cm	45
Long-reach aerial arm	Servo 3 rotation range	°	180
Long-reach aerial arm	Servo 3 stall torque	kg·cm	25
Long-reach aerial arm	Arm weight	kg	1.17
Long-reach aerial arm	Link 1 length	m	0.40
Long-reach aerial arm	Link 2 length	m	0.80
Long-reach aerial arm	Link diameter	mm	5
End-effector	Servo 4 rotation range	°	360
End-effector	Servo 4 stall torque	kg·cm	1.8
End-effector	Maximum gripping diameter	mm	50

The manipulator adopts a three-dimensional serial configuration composed of two lightweight carbon-fiber links measuring 0.40 m and 0.80 m in length, respectively. Both links are rigidly mounted within a dedicated control module positioned beneath the UAV. The entire assembly is structurally integrated with the primary load-bearing frame of the airframe, which suppresses vibration amplification and mitigates undesired structural coupling during flight. Joint actuation was implemented using a HLU-I25 servo motor (JOHO, Shenzhen, China) for Servo 1, a RMU-B50 servo motor (JOHO, Shenzhen, China) for Servo 2, and a RLU-I25M servo motor (JOHO, Shenzhen, China) for Servo 3. Joint positions are obtained through servo-integrated magnetic encoders, enabling closed-loop feedback regulation at the joint level. The end-effector gripper, driven by an MG90S-compatible servo motor, performs object grasping and release tasks, thereby completing the manipulation functionality of the aerial arm.

Based on the identified strong downwash disturbance region, the structural design adopts a dual-configuration strategy: a folded configuration confined within a predefined safety envelope and an extended configuration deployed into the weak-flow region. During takeoff and landing, the manipulator remains fully folded and mechanically locked, with its overall height not exceeding the servo mounting plane. This ensures that the structure does not intrude into the high-momentum rotor downwash core, thereby preserving the nominal aerodynamic profile of the UAV and minimizing aerodynamic coupling effects. During the test, the manipulator actively extends into the reconstructed effective workspace.

The end-effector is positioned outside the strong downwash core region, reducing airflow interference with the target and enhancing manipulation stability, as shown in Figure 17. The full record of the operation process is included in Supplementary Video S2.

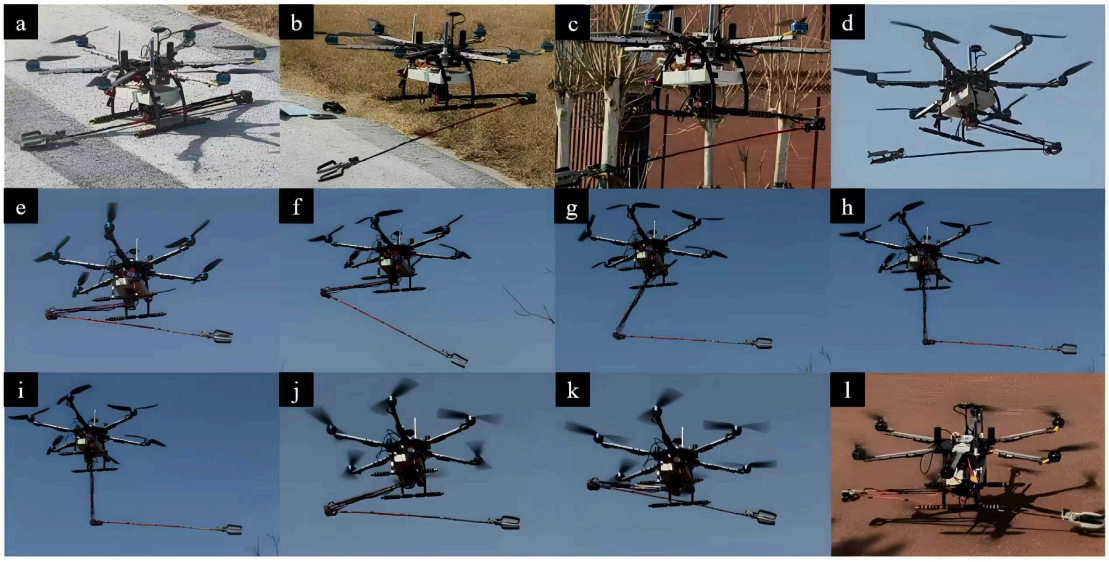

Figure 17. Complete operational process of the aerial arm. (**a**–**d**) show the takeoff phase, (**e**–**h**) present the arm deployment and target grasping process, and (**i**–**l**) depict the arm retraction and landing phase.

Following system integration, a series of outdoor flight experiments were conducted to evaluate the performance of the long-reach aerial arm. The evaluation focused on three primary aspects: (1) stability during takeoff and landing, (2) vehicle attitude response during arm deployment, and (3) end-effector behavior under rotor-induced downwash after full extension.

The experimental results demonstrated that the platform achieved stable takeoff and autonomous landing without external support, such as fixed mounting devices or manual assistance. During these phases, the manipulator remained folded and mechanically locked, thereby preserving the nominal aerodynamic profile and mass distribution of the UAV. Consequently, no specialized infrastructure was required, and the vehicle operated reliably from a standard flat surface. The attitude-control system exhibited no observable overshoot or sustained oscillation during either takeoff or landing.

During hovering, the manipulator was gradually deployed via remote command. Throughout the deployment process, stable hovering was maintained, with no abrupt pitch or yaw deviations observed, and the arm extension remained continuous and well-regulated. To quantitatively evaluate the aerodynamic condition at the end-effector under different arm configurations, a practical threshold of 1 m/s was adopted, below which the rotor-induced airflow was considered sufficiently weak not to interfere with target grasping. As shown in Figure 17g–j, the mean airflow velocities at the end-effector for the four representative grasping configurations were 0.51, 0.25, 0.10, and 0.67 m/s, respectively. All of these values remained below the adopted threshold, indicating that the end-effector had been effectively relocated into a weak-disturbance region where the downwash no longer imposed a significant constraint on target interaction.

By contrast, in the configurations shown in Figures 17e, 17f and 17k, the airflow velocity at the end-effector remained above 1 m/s, with representative values of 2.31, 1.87, and 3.23 m/s, respectively. A similar situation was also observed during the takeoff and landing phases when the manipulator remained in its retracted state. This quantitative contrast demonstrates that the compact or transitional arm configurations are still exposed to relatively strong rotor-

induced disturbance, whereas the fully deployed grasping configurations correspond to a sufficiently weak aerodynamic environment for stable operation. In other words, only after the manipulator is deployed into the reconstructed weak-flow region can the end-effector satisfy the aerodynamic condition required for reliable grasping. These experimental observations are consistent with the flow attenuation characteristics predicted by the CFD simulations. The results validate the core design principle that actively extending the manipulator to relocate the end-effector outside the strong downwash region effectively mitigates aerodynamic disturbance and enhances flight-manipulation stability.

5. Discussion and Conclusions

5.1. Discussion

This study addresses rotor downwash disturbances on manipulation targets in multirotor UAVs and proposes a long-reach aerial arm explicitly designed for aerodynamic avoidance. Unlike conventional compact arms, which prioritize lightweight design and payload capacity, the present approach incorporates the strong downwash region into the design constraints, embedding aerodynamic considerations into structural synthesis.

The framework combines CFD-based flow analysis, workspace reconstruction, and structural optimization, linking aerodynamic characteristics with manipulator configuration and effective operational space. At the theoretical level, a forward-kinematic model of the 3-DOF RRR manipulator was formulated with a geometric height constraint to prevent joints from exceeding the base servo plane in the folded state, thereby preserving aerodynamic safety during takeoff and landing. The strong downwash region was treated as a prohibited domain to truncate the theoretical workspace, yielding an effective operational region with explicit aerodynamic avoidance. This approach surpasses conventional purely geometric reachability analyses by reflecting realistic flight conditions. Moreover, controlled downwash measurements with the UAV laterally fixed on a rigid support frame showed that the CFD-predicted velocity profiles remained close to the experimental mean values and within the corresponding fluctuation bounds, further supporting the reliability of the numerical model used for disturbance-aware workspace design.

Herein, link lengths of 0.40 m and 0.80 m were selected, enabling the end-effector to reach beyond the rotor near-field while remaining compact when folded. At the same time, the selected link-length ratio helps maintain a compact folded configuration in which the manipulator center of mass remains close to the UAV center of gravity, thereby reducing the control burden and improving system stability during takeoff and landing. Flight experiments showed a visually observable reduction in end-effector oscillation tendency after full extension, supporting the feasibility of the long-reach strategy within the tested operating sequence. In this work, 1 m/s is defined as a practical threshold for weak aerodynamic disturbance, and the airflow velocities measured at the end-effector in representative grasping configurations remained below this limit, confirming that the deployed manipulator successfully relocated the operating point into a weak-disturbance region outside the strong downwash core. This suggests that, for contact-based or lightweight harvesting tasks, increased lateral reach can improve operational stability without modifying the flight controller.

The results of this study provide several practical design implications for multirotor-based aerial manipulators. First, the end-effector should avoid persistent operation within the rotor-projected axial high-momentum downwash core. Second, because the induced velocity attenuates more rapidly in the forward and lateral regions, the manipulator workspace should preferably be reallocated forward or laterally rather than being extended only downward. Third, link-length selection should be based not only on geometric reachability but also on CFD-derived flow-field attenuation and the location of weak-disturbance regions. Fourth, the folded configuration should keep the manipulator center of mass as

close as possible to the UAV center of gravity to reduce the attitude-control burden during takeoff and landing. Finally, when further extending the reach of lightweight aerial arms, structural stiffness, payload capacity, joint torque margin, and vibration suppression should be considered together.

The system is implemented on an STM32F411RCT6 microcontroller and validated via manual teleoperation. Its low computational and power demands make it suitable for rapid prototyping. The current control strategy relies on basic position mapping with joint limits; advanced schemes such as force control, impedance control, or perception-driven trajectory control remain future work. Consequently, fully autonomous operation under complex environmental disturbances remains limited.

This work still has several limitations. First, the CFD model is based on a simplified geometry and does not include transient blade-vortex interactions or all detailed airframe structures, which may affect the fidelity of the predicted local flow field. Second, the present aerodynamic analysis mainly considers steady-state flow features and therefore does not fully reflect unsteady wake behavior during actual flight and manipulation. Third, the experimental study is still predominantly qualitative, and quantitative measurements of vibration amplitude, local airflow distribution, and interaction forces have not yet been incorporated. In addition, the current prototype design is not yet fully optimized, and its overall performance remains limited in terms of motion efficiency, structural robustness, and system integration. The current prototype was mainly developed to validate the feasibility of the downwash-aware structural design and workspace-avoidance strategy. Systematic evaluation of the manipulator performance under end-effector payload conditions has not yet been conducted. Due to the long and lightweight arm structure adopted in this study, the current prototype still has limited end-effector payload capacity and is not yet suitable for large payloads or high-precision contact manipulation tasks. Future work will focus on improving the stiffness and payload capacity of the manipulator by optimizing the link cross-section, adopting composite materials with higher stiffness-to-weight ratios, increasing joint torque margins, and introducing mechanical locking or reduction-transmission mechanisms. Tests under different end-effector payload masses will also be conducted to evaluate flight stability, joint torque response, and grasping reliability, thereby establishing a more complete payload-coupled performance evaluation method.

In addition, the long and slender arm structure may introduce flexible vibration. Dedicated modal testing, frequency-response analysis, and vibration-suppression experiments have not yet been conducted in the present study. Therefore, the current results cannot fully quantify the vibration characteristics of the manipulator under the combined effects of rotor-induced airflow, flight-attitude disturbances, and end-effector payloads. Future work will combine modal testing, end-effector acceleration measurement, video-based motion tracking, and finite element structural analysis to quantitatively evaluate the natural frequencies, vibration amplitudes, and damping characteristics of different deployed configurations. From the structural-design perspective, the link-section stiffness, material selection, joint rigidity, and overall assembly stiffness will be improved to reduce vibration risk. From the control perspective, trajectory smoothing, low-frequency resonance avoidance, and vibration-suppression control strategies will be further investigated to improve aerial manipulation stability. Further studies will additionally investigate the performance of the proposed aerial manipulator under more challenging operating conditions, including forward flight, wind disturbances, and dynamic object interaction.

5.2. Conclusions

The main conclusions of this study are summarized as follows:

1. The CFD analysis revealed that the downwash flow generated by the multirotor UAV is spatially nonuniform. A high-momentum axial core exists beneath the rotor-projected region, whereas the induced velocity attenuates more rapidly in the forward and lateral regions. Therefore, the region directly beneath the UAV should be regarded as the main strong-disturbance zone for aerial manipulation.
2. Based on the kinematic model of the 3-DOF RRR manipulator, a theoretical workspace with a geometric height constraint was established. The strong downwash region obtained from the CFD analysis was further introduced as an aerodynamic exclusion zone for workspace reconstruction. Compared with a purely geometric workspace, the reconstructed workspace more realistically reflects the operational envelope of the aerial manipulator under flight-induced aerodynamic disturbances.
3. Considering downwash attenuation, manipulator reachability, and platform stability, link lengths of 0.40 m and 0.80 m were selected. This configuration enables the end-effector to move away from the rotor-projected high-momentum downwash core while maintaining a compact folded configuration with the manipulator center of mass close to the UAV center of gravity.
4. Prototype flight experiments verified the feasibility of the proposed design strategy. In representative grasping configurations, the airflow velocity at the end-effector remained below the adopted weak-disturbance threshold of 1 m/s, indicating that long-reach deployment can effectively reduce the influence of downwash on the end-effector operating region.
5. Future work will incorporate payload-coupled dynamics, vibration testing, force feedback, unsteady CFD simulation, and autonomous perception-control strategies to further improve the stability, robustness, and operational reliability of the aerial manipulation system in complex environments.

Supplementary Materials: The following supporting information can be downloaded at: https://www.mdpi.com/article/10.3390/aerospace13060511/s1, Video S1: Airflow velocity measurement experiment under the fixed-platform condition; Video S2: Full operation process of the long-reach aerial manipulator during the flight test.

Author Contributions: Conceptualization, Z.R. and B.J.; methodology, B.J.; software, B.J. and A.Y.; validation, Z.R., B.J. and X.L.; formal analysis, B.J. and A.Y.; investigation, B.J.; resources, Z.R.; data curation, B.J.; writing—original draft preparation, B.J.; writing—review and editing, Z.R.; visualization, A.Y.; supervision, Z.R. and X.L.; project administration, Z.R.; funding acquisition, Z.R. and B.J. All authors have read and agreed to the published version of the manuscript.

Funding: Excellent Youth Science Fund Project (Overseas) of Shandong Province, China (Grant No. 2023HWYQ-029), China Postdoctoral Science Foundation (Grant No. 2023MD744219), Zhejiang Province Selected Funding for Postdoctoral Research Projects (Grant No. ZJ2023040), Gansu Province Postdoctoral Fund (Grant No. 24JRRA219), Youth Project of Natural Science Foundation of Shandong Province, China (Grant No. ZR2023QE127), Guangdong Basic and Applied Basic Research Foundation (Grant No. 2023A1515110509), Major National Science and Technology Special Project of China (Grant No. 2024ZD1002604) and China National University Student Innovation and Entrepreneurship Development Program (Grant No. 202510422012) have in part supported this research.

Data Availability Statement: All data generated or analyzed during this study are included in this published article and its supplementary information files. Raw data are available from the corresponding author on reasonable request.

Conflicts of Interest: The authors declare no conflict of interest.

References

1. Telli, K.; Kraa, O.; Himeur, Y.; Ouamane, A.; Boumehraz, M.; Atalla, S.; Mansoor, W. A comprehensive review of recent research trends on unmanned aerial vehicles (UAVs). *Systems* **2023**, *11*, 400. [CrossRef]
2. Mendu, B. State-of-the-art review on the application of unmanned aerial vehicles (UAVs) in power line inspections. *Drones* **2025**, *9*, 265. [CrossRef]
3. Sun, J.; Yuan, G.; Song, L.; Zhang, H. Unmanned aerial vehicles (UAVs) in landslide investigation and monitoring: A review. *Drones* **2024**, *12*, 76. [CrossRef]
4. Betti Sorbelli, F.; Corò, F.; Das, S.K.; Pinotti, C.M. UAV-based delivery systems: A systematic review, current trends, and research challenges. *ACM Comput. Surv.* **2024**, *56*, 1–35. [CrossRef]
5. Habibi, S.; Ivaki, N.; Barata, J. A systematic literature review of unmanned aerial vehicles for healthcare and emergency services: Applications, challenges and future directions. *arXiv* **2025**, arXiv:2504.08834.
6. Ghosh, R.; Kim, D. Applications of UAV technologies in assessment of transportation infrastructure systems. *CivilEng* **2025**, *6*, 32. [CrossRef]
7. Barakou, S.C.; Tzafestas, C.S.; Valavanis, K.P. A review of real-time implementable cooperative aerial manipulation systems. *Drones* **2024**, *8*, 196. [CrossRef]
8. Liu, Q.; Lyu, S.; Guo, K.; Wang, J.; Yu, X.; Guo, L. A coordinated framework of aerial manipulator for safe and compliant physical interaction. *Control Eng. Pract.* **2024**, *146*, 105898. [CrossRef]
9. Ruggiero, F.; Lippiello, V.; Ollero, A. Aerial manipulation: A literature review. *IEEE Robot. Autom. Lett.* **2018**, *3*, 1957–1964. [CrossRef]
10. Laiacker, M.; Huber, F.; Kondak, K. High-accuracy visual servoing for aerial manipulation using a 7 degrees of freedom industrial manipulator. In Proceedings of the IEEE/RSJ International Conference on Intelligent Robots and Systems, Daejeon, Republic of Korea, 9–14 October 2016; pp. 7763–7769. [CrossRef]
11. Ollero, A.; Tognon, M.; Suárez, A.; Lee, D.; Franchi, A. Past, present, and future of aerial robotic manipulators. *IEEE Trans. Robot.* **2022**, *38*, 626–645. [CrossRef]
12. Nekoo, S.R.; Suárez, A.; Acosta, J.Á.; Heredia, G.; Ollero, A. Constrained design optimization of a long-reach dual-arm aerial manipulator for maintenance tasks. In Proceedings of the IEEE International Conference on Unmanned Aircraft Systems, Warsaw, Poland, 6–9 June 2023; pp. 1–8. [CrossRef]
13. Suarez, A.; Real, F.; Vega, V.M.; Heredia, G.; Rodriguez-Castaño, A.; Ollero, A. Compliant bimanual aerial manipulation: Standard and long reach configurations. *IEEE Access* **2020**, *8*, 88844–88865. [CrossRef]
14. Sarkisov, Y.S.; Kim, M.J.; Bicego, D.; Tsetserukou, D.; Ott, C.; Franchi, A.; Kondak, K. Development of SAM: Cable-suspended aerial manipulator. In Proceedings of the IEEE/RSJ International Conference on Intelligent Robots and Systems, Macau, China, 3–8 November 2019; pp. 1–8. [CrossRef]
15. Suarez, A.; Salmoral, R.; Garofano-Soldado, A.; Heredia, G.; Ollero, A. Aerial device delivery for power line inspection and maintenance. In Proceedings of the 2022 International Conference on Unmanned Aircraft Systems (ICUAS), Dubrovnik, Croatia, 21–24 June 2022; pp. 30–38. [CrossRef]
16. Jalali, A.; Janabi-Sharifi, F. Aerial continuum manipulation: A new platform for compliant aerial manipulation. *Front. Robot. AI* **2022**, *9*, 903877. [CrossRef]
17. Fernandez, M.J.; Suarez, A.; Ollero, A.; Fumagalli, M. Integration of a variable stiffness link for long-reach aerial manipulation. *arXiv* **2025**, arXiv:2510.15639. [CrossRef]
18. Liu, C.; Li, B.; Wei, Z.; Zhang, Z.; Shan, Z.; Wang, Y. Effects of wake separation on aerodynamic interference between rotors in urban low-altitude UAV formation flight. *Aerospace* **2024**, *11*, 865. [CrossRef]
19. Dougherty, S.; Oo, N.L.; Zhao, D. Effects of propeller separation and onset flow condition on the performance of quadcopter propellers. *Aerosp. Sci. Technol.* **2024**, *145*, 108837. [CrossRef]
20. Tang, Y.; Zhang, Q.; Chen, L.; Li, X. Numerical simulation of the spatial and temporal distributions of the downwash airflow of a multi-rotor UAV. *Comput. Electron. Agric.* **2023**, *206*, 107634. [CrossRef]
21. Chen, H.; Zhao, M.; Li, Y.; Sun, Z. High-resolution numerical investigation of unsteady wake vortices for coaxial rotors. *Chin. J. Aeronaut.* **2024**, *37*, 356–370. [CrossRef]
22. Jin, Y.; Wildmann, N.; Wetz, T.; Beyrich, F. Rotary-wing drone-induced flow: Comparison of simulations with lidar measurements. *Atmos. Meas. Tech.* **2024**, *17*, 2721–2736. [CrossRef]
23. Flem, A.A.; Ghirardelli, M.; Kral, S.T.; Cheynet, E.; Kristensen, T.O.; Reuder, J. Experimental characterization of propeller-induced flow (PIF) below a multi-rotor UAV. *Atmosphere* **2024**, *15*, 242. [CrossRef]
24. De Gregorio, F.; Visingardi, A.; Iuso, G. An experimental-numerical investigation of the wake structure of a hovering rotor by PIV. *Energies* **2021**, *14*, 2613. [CrossRef]
25. Gajo, F.; Heintz, A.; Keßler, M. A comparison of numerical and experimental data from wake decay in hovering rotors. *CEAS Aeronaut. J.* **2025**. [CrossRef]

26. Liu, Y.; Li, D.; Zhao, S.; Xiang, J.; Lu, Y. Aerodynamic analysis of a small-scale propeller under ground-sidewall coupling interference. *Aerosp. Sci. Technol.* **2026**, *170*, 111541. [CrossRef]
27. Morishita, R.; Kawai, S.; Nobuhara, H. Downwash reduction drone with adaptive rotors and its 3D aerodynamic analysis and stabilization control. *IEEE Access* **2024**, *12*, 22832–22840. [CrossRef]
28. Miyahara, K.; Watanabe, R.; Kawai, S.; Nobuhara, H. Structural design and real-world flight verification of a downwash-reducing UAV equipped with adaptive rotors. *IEEE Access* **2025**, *13*, 155003–155014. [CrossRef]
29. Sumathy, V.; Abdul, S.A.M.; Ghose, D. Projection operator-based robust adaptive control of an aerial robot with a manipulator. *J. Field Robot.* **2023**, *40*, 1069–1096. [CrossRef]
30. Zhang, L.; Han, C.; Zhu, Y.; Dong, Y.; Ji, X.; Zhao, Z.; Yang, J. Grasping lightweight objects with Chat-PM: A rotorwash-aware motion planning method. *IEEE Robot. Autom. Lett.* **2023**, *8*, 8114–8121. [CrossRef]
31. Paz, C.; Suárez, E.; Gil, C.; Vence, J. Assessment of the methodology for the CFD simulation of the flight of a quadcopter UAV. *J. Wind Eng. Ind. Aerodyn.* **2021**, *218*, 104776. [CrossRef]
32. Du, S.; Zha, Y. Numerical simulation of the transition flight aerodynamics of cross-shaped quad-tiltrotor UAV. *Sci. Rep.* **2024**, *14*, 17878. [CrossRef]
33. Kostek, A.A.; Lößle, F.; Wickersheim, R.; Keßler, M.; Boisard, R.; Reboul, G.; Gardner, A.D. Experimental investigation of UAV rotor aeroacoustics and aerodynamics with computational cross-validation. *CEAS Aeronaut. J.* **2023**, *15*, 643–658. [CrossRef]
34. Xiang, B.; Tao, G.; Jin, L.; Zhang, J.; Chen, J. CFD aerodynamic analysis of tandem tilt-wing UAVs in cruise flight and tilt transition flight. *Drones* **2025**, *9*, 522. [CrossRef]
35. Scarano, F.; Riethmuller, M. Advances in iterative multigrid PIV image processing. *Exp. Fluids* **2000**, *29*, S051–S060. [CrossRef]
36. Suárez, A.; Sánchez-Cuevas, P.; Fernández, M.; Pérez, M.; Heredia, G.; Ollero, A. Lightweight and compliant long reach aerial manipulator for inspection operations. In Proceedings of the 2018 IEEE/RSJ International Conference on Intelligent Robots and Systems (IROS), Madrid, Spain, 1–5 October 2018; pp. 6746–6752. [CrossRef]
37. Hage, C.; Sophy, T.; Aglzim, E.H. A comprehensive study on the aerodynamic influence of stationary and moving obstacles on an isolated Phantom DJI 3 UAV propeller. *J. Eng.* **2024**, *2024*, e12374. [CrossRef]

Disclaimer/Publisher's Note: The statements, opinions and data contained in all publications are solely those of the individual author(s) and contributor(s) and not of MDPI and/or the editor(s). MDPI and/or the editor(s) disclaim responsibility for any injury to people or property resulting from any ideas, methods, instructions or products referred to in the content.